Journal of Colloid and Interface Science 665 (2024) 793–800

Contents lists available at ScienceDirect

Journal of Colloid And Interface Science

journal homepage: www.elsevier.com/locate/jcis

Regular Article

Cold-plasma activation converting conductive agent in spent Li-ion batteries to bifunctional oxygen reduction/evolution electrocatalyst for zinc-air batteries

Yifan Liu [a], Xiangqun Zhuge [a], Tong Liu [a], Zhihong Luo [b], Kun Luo [a,*], Yibing Li [b,*], Yurong Ren [a], Maryam Bayati [c], Xiaoteng Liu [a,c,*]

[a] Jiangsu Province Engineering Research Centre of Intelligent Manufacturing Technology for the New Energy Vehicle Power Battery, School of Materials Science and Engineering, Changzhou University, Changzhou 213164, PR China
[b] College of Materials Science and Engineering, Guilin University of Technology, Guilin 541004, PR China
[c] Department of Mechanical and Construction Engineering, Faculty of Engineering and Environment, Northumbria University, Newcastle upon Tyne NE1 8QH, UK

HIGHLIGHTS

- ORR/OER catalyst is prepared using discarded Li batteries.
- Cold plasma treatment leads to a larger specific surface area.
- Enhanced catalyst for ORR and OER.
- Zinc-air batteries achieve 640 mAh/g capacity and 92 mW cm^{-2} power density.
- Aqueous zinc-air batteries are capable of stable charge/discharge cycles of 100 h.

GRAPHICAL ABSTRACT

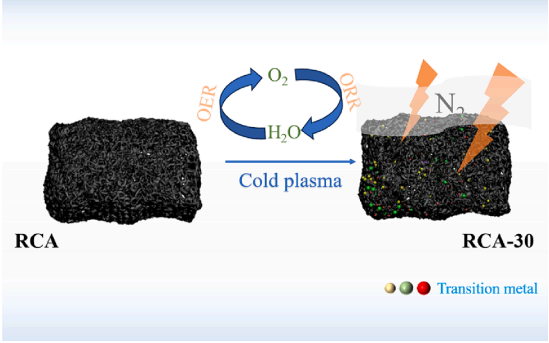

ARTICLE INFO

Keywords:
Conductive agent
Lithium-ion battery
Cold plasma
Activation
Bifunctional catalyst

ABSTRACT

Considerable amount of high-value transition metals components can be recycled in spent ternary lithium-ion batteries. In this study, we utilized the conductive agent carbon black, obtained from the leaching waste resulting from the chemical recovery of spent lithium-nickel-manganese-cobalt (NCM) oxide cathode materials. This process allows us to create valuable bifunctional catalysts for the oxygen reduction reaction and oxygen evolution reaction (ORR/OER), facilitated by a facile cold plasma activation method, as a part of lithium batteries circular economy. The activated conductive agent (RCA-30) exhibited an ORR half-wave potential of 0.74 V (vs. RHE) in 0.1 mol/L KOH solution, and an OER overpotential of 360 mV at 10 mA cm^{-2} in 1 mol/L KOH electrolyte, owing to nitrogen doping of carbon black and activation of surface metal oxides. The complete zinc-air batteries incorporating the activated catalysts at the cathode exhibited an open circuit potential of up to 1.48 V and sustained cycling for 100 h at a current density of 5 mA cm^{-2}. Additionally, the activated catalysts contributed to a power density of 92 mW cm^{-2} and a full discharge capacity of 640 mAh/g.

* Corresponding authors at: Jiangsu Province Engineering Research Centre of Intelligent Manufacturing Technology for the New Energy Vehicle Power Battery, School of Materials Science and Engineering, Changzhou University, Changzhou 213164, PR China (X. Liu).
E-mail addresses: luokun@cczu.edu.cn (K. Luo), lybgems@glut.edu.cn (Y. Li), terence.liu@northumbria.ac.uk (X. Liu).

https://doi.org/10.1016/j.jcis.2024.03.169
Received 1 December 2023; Received in revised form 4 March 2024; Accepted 25 March 2024
Available online 26 March 2024

1. Introduction

Lithium nickel-manganese-cobalt (NCM) oxide batteries integrate the advantages of the three primary elements in the cathode. While nickel alone boasts high specific energy, it lacks stability [1,2]. In contrast, manganese is exceptionally stable but has a lower specific energy. Their combination results in a chemically stable composition with high specific energy. As the battery capacity diminishes to 80 %, lithium-ion batteries (LIBs) no longer meet the power cell requirements for electric vehicles and must undergo recycling upon retirement. Spent NCMs are enriched with lithium, nickel, cobalt, and manganese elements, underscoring the significant economic and non-renewable natural resource utilisation benefits of chemical recycling [3–5]. However, the high-value conductive agents in the leaching residues continue to be treated as solid waste due to contamination during battery cycling.

Different from typical nanocarbon materials, the conductive agents utilised in LIBs demand a higher standard in terms of metal impurity content and oil absorption value, resulting in high cost compared to conventional carbon blacks. Notably, conductive agents like Super P (SP) and Cochin Black can achieve oil absorption values of at least 250 mL g^{-1}, with their branch-like aggregates enhancing conductive contact with cathode materials. In contrast, ordinary carbon blacks only exhibit an absorption value of 180 mL g^{-1}. During the chemical recovery process of spent cathode materials, the conductive agents typically persist in the leaching residual [6,7]. The projected volume of retired LIBs is estimated to surpass 11 million tons by 2030, marking the onset of the initial retirement wave [8–10]. Consequently, the recycling of conductive agents holds substantial economic benefits.

It is recognised that conductive agents, after undergoing battery cycling, become contaminated and fail to meet specifications for reuse in LIBs. But, the contamination either in form of residual transition metals (Ni, Co, Mn) oxides or as doping heteroatoms imparts significant catalytic capabilities to the spent conductive agents, particularly in ORR/OER. Ni, Co and Mn oxides are known to exhibit oxygen electrocatalysis, owing to their variant oxidation states, structural diversity, moderate conductivity and robust stability [11,12]. By rational combination, Ni, Co, and Mn oxides can also possess both ORR and OER dual functional activities [13]. The introduction of transition metal atoms into nitrogen-doped nanocarbon materials can yield ORR/OER bifunctional electrocatalytic performance comparable to that of noble metal catalysts [14–16]. When combined with carbon substrates, the electronic conductivity is further improved. Notably, this is the exact state in which the conductive agent is being recycled.

Zinc-air batteries (ZABs) have received increasing attention for their application in as power source for wearable electronic devices as well as electric vehicles due to high specific energy density (1084 Wh kg^{-1}), low cost and safety [18,19]. The performance and cost of ZABs hinge significantly on the air cathode, which serves as a crucial component. Highly active ORR/OER catalysts are required for the cathode, thereby it plays a vital role in the overall battery functionality. The surface wettability of the cathode also reported to exert important effect on the performance of ZABs by Tang et al. [20]. In terms of ORR/OER catalysts made from waste materials, Jiao et al. used a fast thermal radiation method to convert the cathode of a waste lithium ternary battery into an efficient NiCoMn-based ZABs catalyst. This one-step catalyst preparation method is low cost and the ZABs showed an excellent power density (187.7 mW cm^{-2}) [21]. Zhou et al. used a wet recycling method to recover iron phosphate from used lithium iron phosphate batteries and calcined the filter slag with the recovered iron phosphate in N_2 atmosphere at high temperatures to form a Fe-N-P co-doped carbon catalyst. The catalyst also exhibited a power density of 80 mW cm^{-2} when applied to aqueous ZABs [17].

Drawing inspiration from these findings, this paper explores the transformation of $LiNi_{0.7}Co_{0.15}Mn_{0.15}O_2$ (NCM-701515) recycled conductive agent into a highly efficient catalyst cathode for ZABs. The conductive agent after chemical recovery of NCM-701515 was treated by nitrogen cold plasma, achieving dual benefits of reducing environmental pollution and substantially reduced the catalyst cost of ZABs. Cold plasma can generate high-energy electrons and active species at room temperature. It has been demonstrated as a rapid, straightforward, and environmentally friendly method for catalyst preparation, performance alternation and enhancement [22]. Plasma bombardment can enlarge the surface area of materials, expose active sites, and thus improve catalytic performance [23]. The energy of plasma can be strong enough to enable nitrogen doping in N_2 [24] or NH_3 [25] atmospheres. Tian et al. reported to successfully introduce atomic dispersed Fe and N into carbon (SAC-Fe/NC) by plasma bombardment. These SAC-Fe/NC catalysts displayed an impressive electrochemical performance with a high half-wave potential (vs. RHE) of 0.92 V. When utilised as an air cathode in ZABs, they exhibited a remarkable power density of 263 mW cm^{-2} and a specific capacity of 803 mAh/g, surpassing that of Pt/C-based ZABs [26]. Cold plasma also assists uniform deposition of catalysts. Liu et al. used cold plasma to uniformly deposit Pt@Pd onto antimony tin oxide (ATO). The obtained Pt@Pd/ATO catalyst exhibited higher ORR performance than commercial Pt/C, and the electrochemical life test showed dramatically improved durability [27].

In this study, we demonstrate that direct cold plasma treatment at low nitrogen pressure enables the nitrogen doping of the recovered conductive agent (RCA) in spent LIBs and activation of residual Ni, Co, Mn oxides on the surface, rendering them efficient ORR/OER bifunctional electrocatalysts and used for ZABs. The NCM-701515 cathodes were separated from spent LIBs and the high-value elements of Li, Ni, Co and Mn were chemically recycled, achieving recovery rates exceeding 99 % for all four elements. In addition, the conductive agents in the leaching residual were also recycled, which demonstrated notable ORR/OER bifunctional catalytic performance after plasma bombing. Consequently, the electrochemical performance of ZABs saw significant improvement, showcasing the potential applicability of these catalysts in other metal-air batteries, water splitting, fuel cells, and supercapacitors as cost-effective alternatives.

2. Experimental

2.1. Materials and chemicals

Sulfuric acid (H_2SO_4, 95.0–98.0 %), hydrogen peroxide (H_2O_2, 30.0 % solution), anhydrous ethanol (CH_3CH_2OH, ≥99.7 %), isopropanol ($(CH_3)_2CHOH$, ≥99.7 %), acetone (CH_3COCH_3, ≥99.5 %), perfluorinated resin (Nafion, 5 wt% in mixture of lower aliphatic alcohols and water), zinc acetate dihydrate ($Zn(AC)_2{\cdot}2H_2O$, ≥99.0 %), sodium chloride (NaCl, ≥99.5 %) were bought from China National Pharmaceutical Chemical Reagent Co., Ltd. Potassium hydroxide (KOH, ≥90.0 %), ruthenium oxide (RuO_2, ≥99.9 %), JM 20 % platinum carbon (20 % Pt/C, HISPEC 3000) were purchased from Adamas Chemical Co., Ltd. Spent ternary $LiNi_{0.7}Co_{0.15}Mn_{0.15}O_2$ (NCM-701515) batteries were obtained from Gotion High-Tech Co., Ltd., and Super P (SP, Vulcan XC-72, 12.01 MW) was purchased from Shanghai Macklin Biochemical Technology Co., Ltd. Aqueous solutions were prepared in deionized water (ionic conductivity < 0.055 μS cm^{-1}).

2.2. Recycling of spent ternary cathode materials

The spent ternary LIBs were discharged in 0.5 mol/L NaCl solution for 24 h, which were then manually disassembled in a fume hood to obtain the cathode material directly. The cathode material was subsequently heated at 400 °C to decompose the organic binder in the cathode, and then separated the NCM-701515 powders from the aluminum foil substrate. 5 g of the powders were dispersed in 250 mL of 1 mol/L H_2SO_4 solution at 50 °C, and then 6 mL of 2 vol% H_2O_2 was added and kept stirring for 50 min. The leaching approach to recovery Li, Ni, Co and Mn elements followed our previous work [6], and the leaching residual was separated and dried at 60 °C for 8 h, led to the recovered conductive agent named as RCA.

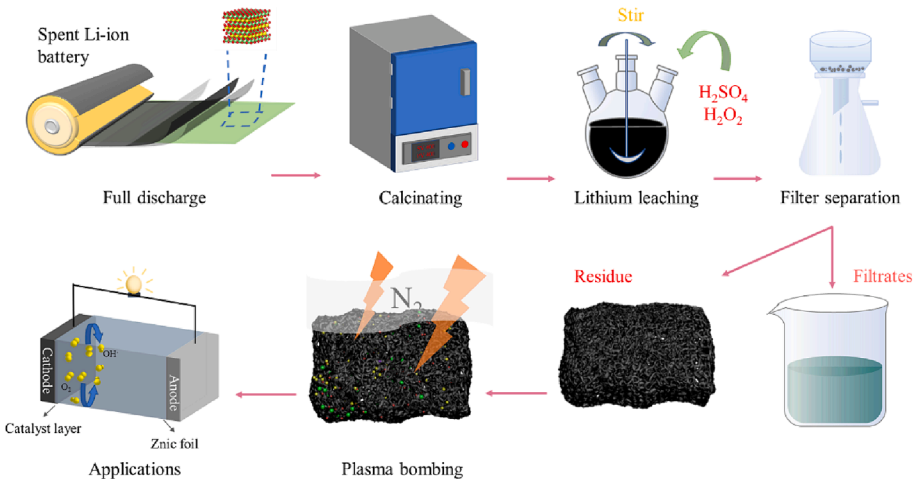

Scheme 1. Recovery and cold plasma activation of conductive agents in spent ternary cathode materials.

The powders were placed in an air-proof container, which was filled with pure N_2 at a low pressure of 100 Pa. A Tesla coil was used to excite cold plasma in the container, and the RCA was treated for 15 min and 30 min, respectively, marking as RCA-15 and RCA-30. As reference, the pristine SP was also treated in the same manner, and the samples treated for 15 min and 30 min were noted as SP-15 and SP-30. The whole process is illustrated in Scheme 1.

2.3. Assembly and testing of ZABs

A rechargeable ZAB was in use equipped with a zinc plate (>99.9 %) anode and a composite cathode substrate (Changsha Spring New Energy Technology Co., Ltd.) sprayed with the catalyst slurry for testing. 10 mg of the catalyst was sonicated for 30 min in a mixture of 100 μL of 5 % Nafion solution, 975 μL of isopropanol and 975 μL of deionized water, resulted in the catalyst slurry. The composite substrate was sprayed with the catalyst slurry at a loading of 0.4 mg cm^{-2} and dried at 60 °C for 8 h. An aqueous electrolyte solution was used containing 6.0 mol/L KOH and 0.2 mol/L $Zn(Ac)_2$.

A battery testing system (LAND CT2001A) was used to test the assembled ZABs. The cut-off voltage for testing the cyclic performance was set up from 0.5 V to 2.5 V, where the ZABs were discharged and charged separately for 20 min each at the current density of 5 mA cm^{-2}. The full-discharge testing was also carried out at 5 mA cm^{-2} and stopped at 0.6 V. Rate performance of the ZABs were recorded following the sequence from 1 mA cm^{-2} to 5 mA cm^{-2}, 10 mA cm^{-2}, 20 mA cm^{-2}, 30 mA cm^{-2}, and finally ended up at 5 mA cm^{-2}, and the discharge duration was settled as 10 min for each test. The polarization curves and the open-circuit voltages (OCVs) were measured using the electrochemical workstation with a sweep rate of 5 mV s^{-1}.

2.4. Characterizations

The contents of Ni, Co, Mn and Li elements in solid samples were determined with an inductively coupled plasma-optical emission spectrometer (ICP-OES, OPTIMA 8000, Perkin Elmer). XRD and Raman analyses were carried out on a Bruker D8 Advance diffractometer (Cu-Kα λ = 1.5406 Å) and a DXR2 Raman Microscope (532 nm). The morphology of the samples was characterized by a field emission scanning electron microscope (FESEM, SEU8010), transmission electron microscopy (TEM, Thermo Scientific Talos F200X G2, 100 kV) and high-angle annular dark-field scanning transmission electron microscope (HAADF-STEM, JEM-ARM200 F TEM/STEM, 200 kV). An X-ray photoelectron spectroscope (XPS, ESCALAB 250Xi, Thermo Fisher Scientific) was used to analyze the surface chemistry, and the particle size and specific surface area were measured by a Micromeritics ASAP 2460 Surface Area and Porosity Analyzer with Brunauer-Emmett-Teller (BET) method. Electrochemical analysis was described in the Supporting Information (SI).

3. Results and discussion

3.1. Structural characterizations

The recycling method of spent ternary LIB cathode materials is shown in Scheme 1. **Table S1** in the SI shows the results of ICP-OES analysis, where the percentages of Li, Ni, Co and Mn in the spent ternary cathode were 6.2 %, 39.2 %, 8.6 % and 8.9 %, respectively. After calcined at 400 °C, the cathode material was chemically leached with 1 mol/L H_2SO_4 and H_2O_2 solution, and Li^+, Ni^{2+}, Co^{2+} and Mn^{2+} were dissolved in the solution, which were recovered by the approach described in our previous work [6]. **Table S1** also show existence of the transition metal elements in the filtering residual, and the leaching rates of Li, Ni, Co and Mn were calculated as 99.61 %, 99.37 %, 99.28 %, and 99.15 %, respectively. Thus, the remaining Li, Ni, Co, and Mn contents in the RCA were only 0.03 %, 0.27 %, 0.06 %, and 0.06 %, respectively.

Fig. S1 shows the SEM image of the NCM-701515, which shows the uneven, transverse, and longitudinal material surface, and the energy-dispersive EDX of the NCM-701515 indicates presence of C, O, Ni, Co, and Mn elements. **Fig. S2a** and **S2b** compares the morphological change after cold plasma treatment, in which the SEM image of the RCA exhibits a smooth surface, but the RCA-30 after treated for 30 min displays a loose and porous structure. The same phenomenon was also observed for the SP. As illustrated in **Fig. S3**, the SP-30 after treated for 30 min also shows a loose and porous morphology, illustrating the physical effect of cold plasma on the surface of materials.

Fig. 1**a** presents a HRTEM image of RCA-30, with an inset displaying a SAED pattern. Through lattice spacing measurements, we identified streaks exhibiting two distinct lattice spacings: 0.25 nm and 0.43 nm. These measurements correspond with the (200) and (222) crystal planes of the NiO crystal, respectively. In the SAED map inset of Fig. 1**a**, analysis was conducted to identify the crystal faces associated with the diffraction circles, specifically (200) and (222), which also correspond to NiO. **Fig. S4** shows TEM images of RCA-30 and RCA at various magnifications. By annotating and measuring **Fig. S4f**, the observed lattice spacing was determined to match the (111) and (222) crystal planes of NiO. Additionally, it is evident that RCA exhibits superior crystallisation. This further confirms that nitrogen-cooled plasma treatment leads to weakened crystallinity of the crystals. The high-angle annular dark-field scanning transmission electron microscopy image (HAADF-STEM) of the RCA-30 in Fig. 1**b** further illustrates the presence of Ni, Co, Mn oxides on the carbon substrate. The element mapping in

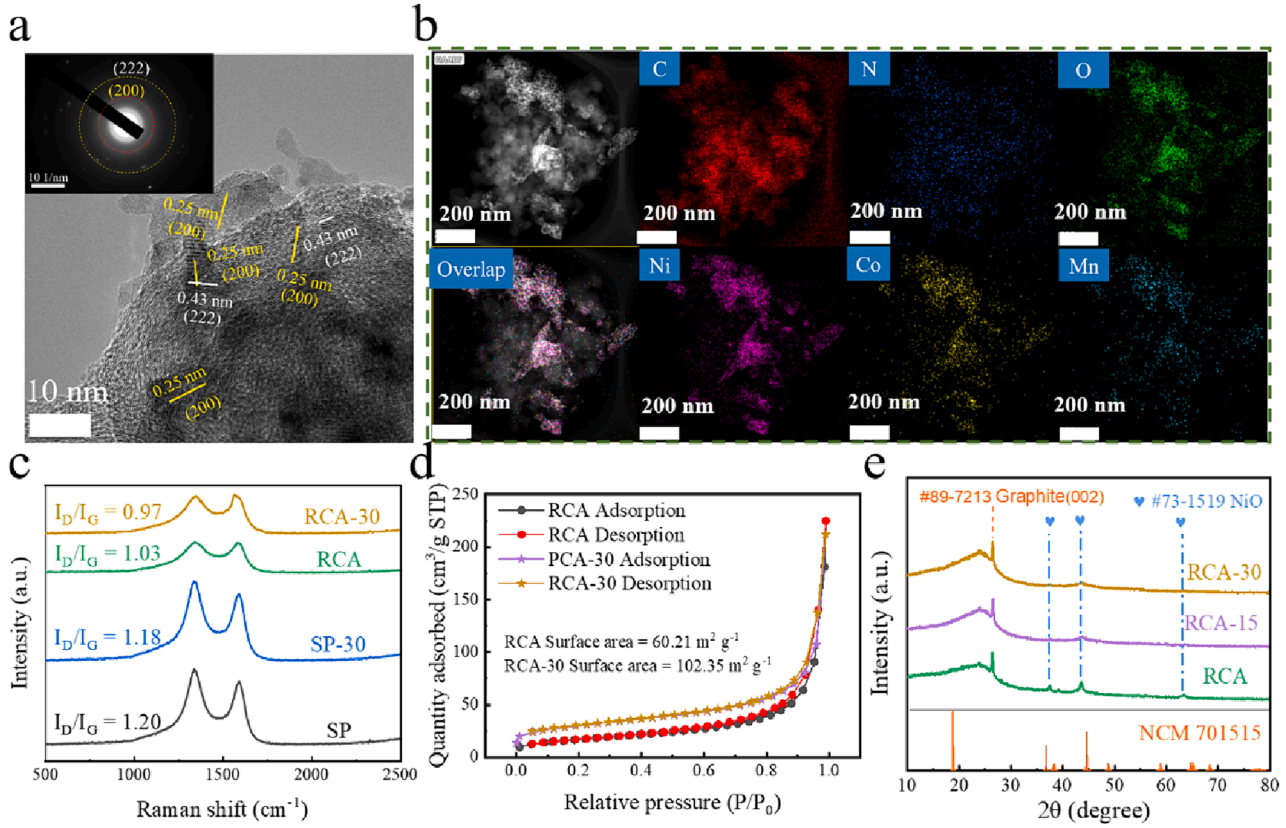

Fig. 1. High-resolution transmission electron microscopy (HRTEM) (a) and Selected Area Electron Diffraction (SAED) pattern (inset) of the RCA-30, HAADF-STEM image and element mapping (b) of the RCA-30, Raman analyses (c) of the RCA, RCA-30, SP and SP-30, N_2 adsorption/desorption isotherms (d) of the RCA and RCA-30, and XRD analyses (e) of the RCA, RCA-15 and RCA-30.

Fig. 1**b** distinctly displays the local concentrated O, Ni, Co, and Mn species, indicating the presence of Ni, Co, Mn oxides on the carbon substrates (also ref. the overlap image). In contrast, the distribution of N is quite uniform, exhibiting a homogeneous nitrogen doping of the carbon substrates.

Fig. 1**c** shows the Raman profile of the samples, where the disorder peak (D) at 1347 cm^{-1} and graphite peak (G) at 1588 cm^{-1} are observed. The intensity ratio of the D peak to the G peak (I_D/I_G) can be used as an indicator to quantify the degree of graphitization [28,29], where the I_D/I_G values of the RCA and RCA-30 were 1.03 and 0.97, and of the SP and SP-30 were measured as 1.20, 1.18, respectively. The increase on the degree of graphitisation after cold plasma bombardment for these two types of carbon black samples helps to improve the electron conductivity of the materials. Fig. 1**d** shows that RCA and RCA-30 exhibit type IV isotherms in N_2 adsorption/desorption tests with specific surface areas of 60.21 m^2/g and 102.35 m^2/g respectively, illustrating that the specific surface area of the conductive agent becomes significantly larger after nitrogen cold plasma treatment. The reference SP as displayed in **Fig. S5a** has a much larger specific surface area of 383.78 m^2/g than the RCA, and **Fig. S5b** illustrates the specific surface area further increases to 412.47 m^2/g after cold plasma bombardment (i.e. SP-30), highlighting the increase of surface area owing to the cold plasma bombardment in agreement with the morphological evolution shown in **Fig. S2a** and **S2b** as well as **Fig. S3a** and **S3b**.

XRD spectrum of the cathode material (blue) from spent LIBs displays the characteristic peaks of NCM-701515 crystal (black) in **Fig. S6,** indicative of the content of the cathode material. **Fig. S7** shows the XRD results of the SP and SP-30, where the peaks at 24.8° and 43.3° correspond to the (002) and (101) plane (PDF# 89-7213), in line with previous literature [30]. As for the RCA in the leaching residual, Fig. 1**e** compares the diffraction patterns of RCA, RCA-15 and RCA-30, which exhibits less peaks intensity in comparison to the typical NCM-701515 crystal (black) in **Fig. S6**, suggesting that very small amount of the Ni, Co, and Mn oxides are remained on the carbon substrate, in agreement with the high recovery rates (**Table S1**). A strong peak at 26.6° appears in all the three samples, assigned to the (002) plane of graphite (PDF# 89-7213). Moreover, three small peaks are found at 37.3°, 43.4° and 63.2°, attributed to the (111), (200), (220) facets of NiO crystal (PDF#73-1519). This can be assigned to the oxide content in the RCA, where Ni (0.27 %) is nearly fivefold of Co (0.06 %) and Mn (0.06 %), and therefore can be regarded as Co, Mn doped NiO, marked as CMNO in the following content. We processed the peak widths XRD and calculated the particle size of the material under different conditions according to Debye-Scherrer formula. As shown in **Table S2**, the particle size of RCA-30 is 3.21 nm, which is much smaller than that of RCA of 9.93 nm. It indicates that the grain size of the material gradually decreased with the duration of nitrogen-cooled plasma treatment.

X-ray electron spectroscopy (XPS) analysis in Fig. 2**a** illustrates the total spectrum of the RCA-30, where the signals of C, N, Ni, Co and Mn are seen. Fig. 2**b** shows the fitting of the high resolution C1s spectrum, which manifests four peaks of C-C (284.8 eV), C-O (285.5 eV), C-N (287.7 eV), and C=O (291.5 eV). The presence of C-N bond in the RCA-30 after nitrogen cold plasma treatment manifests the difference with the RCA (see **Fig. S8a),** and the cold plasma treatment also brings with an additional C-N bond for the SP-30 in comparison with the C1s spectrum of the pristine SP in **Fig. S8b**. N1s spectrum in Fig. 2**c** confirms *N*-doping. The high resolution N1s spectrum of the RCA-30 can be fitted in the four peaks attributed to pyrrole N (398.7 eV), pyridine N (400.1 eV), graphite N (401.2 eV), and oxidized N (405.1 eV), respectively **(**Fig. 2**c).** The pyridine N is considered to be the active component that enhances the electron-donating ability to promotes ORR, and graphite N is regarded to be the active component that increases the current density

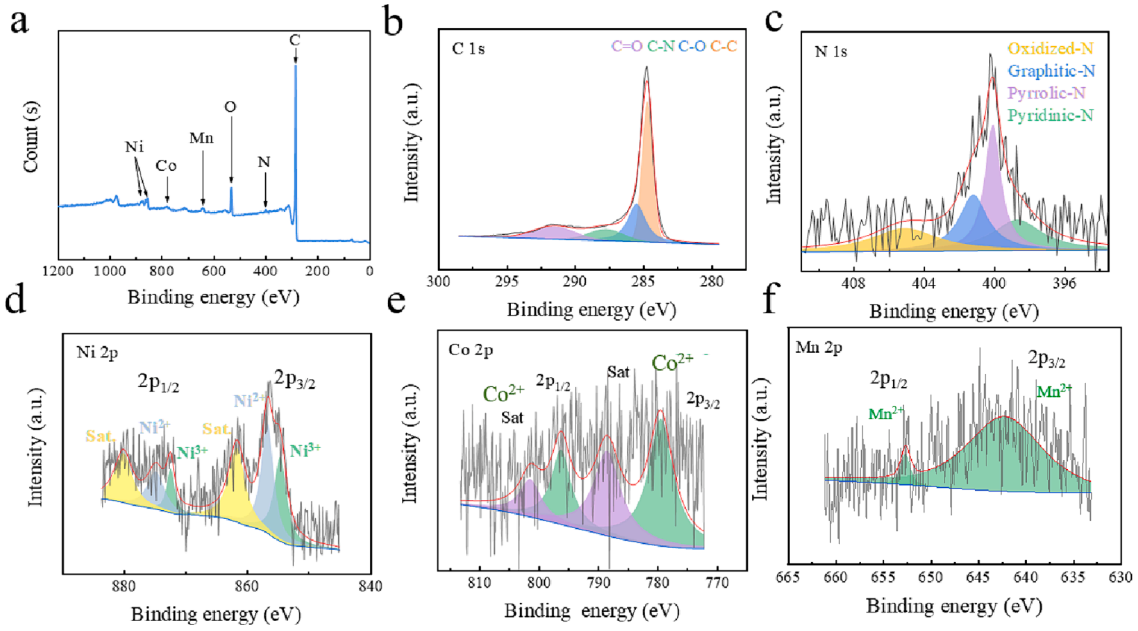

Fig. 2. The XPS (a) full, (b) C 1s, (c) N 1s, (d) Ni 2p, (e) Co 2p and (f) Mn 2p spectrum of RCA-30.

[31,32]. The high-resolution XPS spectra of Ni_{2p} (Fig. 2**d**) signals can be split into $2p_{3/2}$ peaks and $2p_{1/2}$ peaks due to spin–orbit coupling. The fitted XPS spectra of Ni_{2p} located at 856.9 eV and 874.7 eV correspond to Ni^{2+}, while the peaks located at 854.7 eV and 872.4 eV are associated to the Ni^{3+} oxidation state. In addition, two satellite peaks, located at 861.6 eV and 880.1 eV, correspond to the spin–orbit peaks of the Ni^{2+} oxidation state [33,34]. The signal of Co $2p_{3/2}$ is located at 779.4 eV, and the peak of Co $2p_{1/2}$ appears at 796.2 eV, together with satellite peaks at 788.4 eV and 801.4 eV, corresponding to Co^{2+} oxidation state [35]. Presence of Mn^{2+} oxidation state can be found out from the binding energies at 642.3 eV and 652.7 eV attributed to Mn $2p_{3/2}$ and Mn $2p_{1/2}$ [36]. XPS data tabulated in **Table S3** shows no signal for the existence of M (Ni, Co, Mn)-N-C bonds.

3.2. *Electrocatalytic properties*

The half-cell ORR performance of the catalyst-modified glassy carbon electrodes (GCEs) was tested in 0.1 M KOH electrolyte at room temperature in comparison to the commercial 20 % Pt/C catalysts (simplified as Pt/C). As shown in **Fig. S9**, the electrochemical active area (ECSA) of the RCA-30 (9.41 mF cm^{-2}) was increased compared to SP-30 (8.83 mF cm^{-2}) and RCA (3.69 mF cm^{-2}) for the bilayer capacitance analysis. **Fig. S14a** and **S14b** illustrates that the ECSA of the RCA-15 is 4.89 mF cm^{-2}, situating between the RCA and RCA-30. **Fig. 3a** displays the CV curves of the GCEs modified with the SP-30, RCA, RCA-30 and Pt/C catalysts, where the ORR peak currents of 0.32, 0.42, 0.58 and 0.73 mA cm^{-2} appear at 0.69 V, 0.65 V, 0.68 V and 0.68 V, respectively.

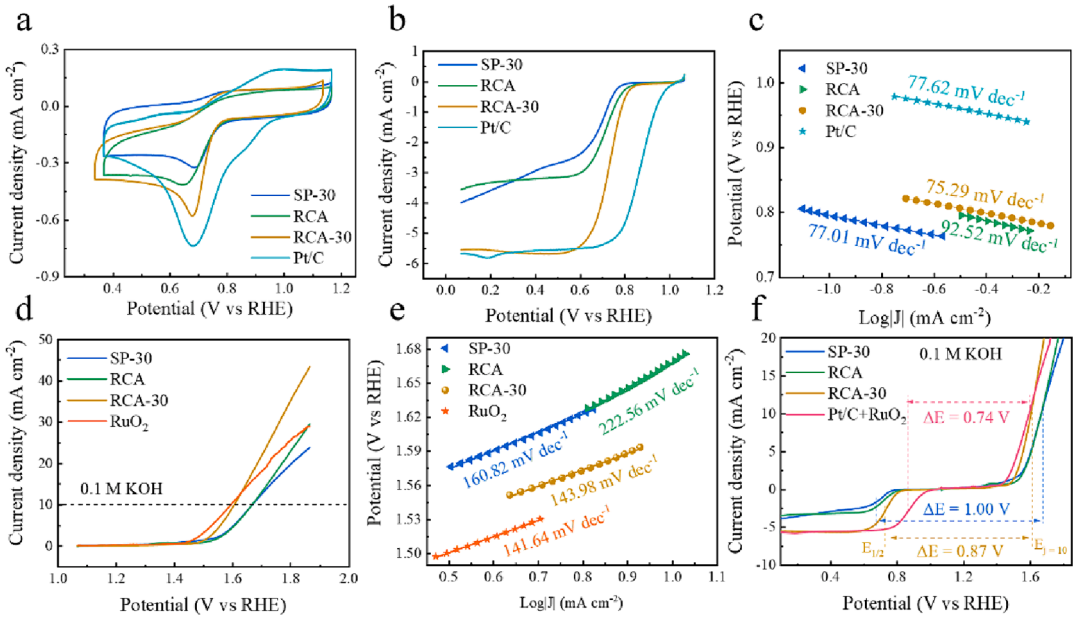

Fig. 3. Electrocatalytic performance of the SP-30, RCA, RCA-30 in 0.1 M KOH solution in comparison with the Pt/C in ORR and RuO_2 in OER: (a) cyclic voltammograms; (b) ORR polarisation curves at 1600 rpm; (c) Tafel plots in ORR at 1600 rpm; (d) OER polarisation curves; (e) Tafel plots in OER; (f) Overall polarisation curves.

Compared with the RCA and RCA-30, the catalytic current of SP-30 is even weaker than the RCA due to the presence of CMNO on the surface, although the latter owns larger active area, and after plasma treatment the RCA-30 is even more active, but is still weaker than the Pt/C.

The linear sweep voltammetry (LSV) analysis using RDE at 1600 rpm in Fig. 3**b** shows that the half-wave potentials of the RCA-30 catalyst is 0.74 V vs. RHE, with the diffusion current density of 5.5 mA cm^{-2}. In contrast, the half-wave potentials of the SP-30, RCA and Pt/C are 0.68, 0.71 and 0.87 V, respectively, with a diffusion current density of 4.0, 3.6 and 5.5 mA cm^{-2}. Moreover, the Tafel slope of the RCA-30 is 75.29 mV dec^{-1}, and the value of SP-30, RCA and 20 % Pt/C are 77.01, 92.52 and 77.62 mV dec^{-1}(see Fig. 3**c**). **Fig. S14c** illustrates that the half-wave potential of the RCA-15 is at 0.67 V with the diffusion current density of 4.8 mA cm^{-2}, and the inset reveals the Tafel slope of the RCA-15 is 82.56 mV dec^{-1}, which stays between the RCA and RCA-30 as well. It is seen that the RCA-30 exhibits comparable diffusion current density and Tafel slope with the Pt/C under convective mass transfer conditions. Stability of the RCA, RCA-30, and SP-30 was tested for ORR using chronoamperometry method at a constant voltage of -0.2 V vs. Hg/HgO. As shown in **Fig. S10**, RCA-30 still maintained a high relative current of 70.2 % after 35,000 s. In comparison, the current density retention of SP-30 and RCA was only 55.1 % and 33.9 % under the same conditions. The results indicate that cold plasma treatment effectively enhance the catalytic activity and long-term durability of the RCA, with potential for practical application as an ORR catalyst in devices.

RDE analysis of the RCA-30 is shown in **Fig. S11** from 400 to 1600 rpm, with the limit current density increasing as the speed increases. **Fig. S11** inset shows the RCA-30 curve fitted to the *Koutecky-Levich* (K-L) plots. The results based on the linear K-L plot show that RCA-30 is a 4-electron pathway with an electron transfer number of approximately 3.9. This is consistent with the results of the rotating ring disc electrode (RRDE) electron transfer number test (**Fig. S12**), which showed that the electron transfer number of the RCA-30 catalyst was 3.8 at 0.07 V (RHE), higher than the SP-30 and RCA. In addition, the RCA-30 catalyst corresponded to a relatively low leaching rate of H_2O_2, which provides even stronger evidence that the RCA-30 catalyst is a 4-electron transfer catalyst.

The OER performance of the SP-30, RCA and RCA-30 was also tested in comparison with the RuO_2 catalyst. Fig. 3**d** shows the OER LSV curves for the three catalysts in 0.1 M KOH electrolyte at a scan rate of 5 mV s^{-1}. The RCA-30 catalyst exhibits excellent OER catalytic activity, yielding a voltage of merely 1.61 V at a current density of 10 mA cm^{-2}. The associated overpotential is 378 mV, which is lower than those of the SP-30 (440 mV) and RCA (437 mV), but is higher than the RuO_2 catalyst (360 mV). Fig. 3**e** displays that the Tafel slope of the RCA-30 (143.98 mV dec^{-1}) is also smaller than the SP-30 (160.82 mV dec^{-1}) and RCA (222.56 mV dec^{-1}), and slightly larger than that of RuO_2 (141.64 mV dec^{-1}). Similarly, **Fig. S14d** illustrates that a voltage of 1.65 V was generated for the RCA-15 at the current density of 10 mA cm^{-2} with a corresponding overpotential of 420 mV, indicating the effect of cold plasma treatment on the OER catalytic activity of the RCA. With the electrolyte concentration increased to 1 mol/L KOH, **Fig. S13a** shows that the RCA-30 catalyst presents better catalytic activity with onset voltage of 1.59 V at a current density of 10 mA cm^{-2}. The associated overpotential decreases to 360 mV, which is lower than SP-30 (420 mV) and RCA (450 mV) but slightly higher than that of RuO_2 catalyst (330 mV). The Tafel slope of the RCA-30 (144.08 mV dec^{-1}) in 1 M KOH solution is significantly smaller than those of the SP-30 (148.37 mV dec^{-1}) and RCA (156.55 mV dec^{-1}), but is larger than that of RuO_2 (106.94 mV dec^{-1}), as shown in **Fig. S13b**.

The overall oxygen electrode performance was evaluated by ΔE (E_{OER}-E_{ORR}), which is the difference between the OER potential at 10 mA cm^{-2} and the ORR half-wave potential. As shown in Fig. 3**f** and **Fig. S14c**, the ΔE values for RCA-30, SP-30, RCA-15, and RCA are measured as 0.87, 1.00, 0.95, and 0.96 V, respectively. It is clear that the RCA-30 owns the optimal bifunctional catalytic performance among SP-30, RCA and RCA-15, but is still weaker than the combination of 20 % Pt/C + RuO_2 (ΔE = 0.74 V). **Table S4** lists previous carbon-based bifunctional catalysts in the literature, and the RCA-30 catalyst can match the performance of these catalysts in 0.1 M KOH solution.

To determine the potentially electrocatalytically active species in the materials, we initially treated the RCA materials with aqua regia acid leaching, during which the transition metal materials were fully leached out and designated as A-RCA. Following this, we applied a nitrogen-cooled plasma treatment to the samples, which were then labeled as *N*-A-RCA. The electrocatalytic performances for the Oxygen Reduction Reaction (ORR) and the Oxygen Evolution Reaction (OER) are depicted in **Fig. S16**. **Fig. S16a and S16b** show the LSV curves for the ORR and the associated Tafel plots. It is observed that the current density, half-wave potential ($E_{1/2}$), and Tafel slope for A-RCA are lower compared to RCA, indicating poorer ORR performance for A-RCA. Following nitrogen-cooled plasma treatment, the ORR performance of *N*-A-RCA showed improvement, though it remained less effective than that of RCA. **Fig. S16c** illustrates the OER performance in 0.1 M KOH solution, noting that A-RCA's current density failed to achieve the benchmark of 10 mA cm^{-2}. **Fig. S16d** and its inset detail the OER LSV curves and corresponding Tafel plots in 1 M KOH solution, highlighting that both the overpotential and Tafel slope of A-RCA are lower than those of RCA. The nitrogen-cooled plasma treatment enhances the OER performance of *N*-A-RCA, yet it still does not match the OER capability of RCA. In conclusion, the analysis suggests that transition metal oxides are the primary catalytic species within the material, and that nitrogen-cooled plasma treatment aids in boosting both ORR and OER performances.

3.3. *Rechargeable Zn-air batteries*

The application of the RCA-30, SP-30 and RCA as cathode catalysts in rechargeable ZABs was also investigated in comparison to the combination of the Pt/C and RuO_2. Fig. 4**a** displays the open circuit voltages (OCVs) of the ZABs with the catalysts, in which the ZAB with the RCA-30 catalyst exhibits the same OCV value of 1.45 V as the one with the Pt/C + RuO_2 (1.45 V), apparently higher than those using the SP-30 (1.37 V) and RCA (1.38 V) catalysts. The RCA-15 based ZAB has an open-circuit voltage of 1.42 V (**Fig. S15a**), which is also better than the one with the RCA.

Fig. 4**b** illustrates the rate performance at different discharge current densities ranging from 1 mA cm^{-2} to 30 mA cm^{-2}. The ZAB with the Pt/C + RuO_2 catalyst exhibits the best performance, followed by the one with the RCA-30. The ZABs with the SP-30, RCA-15 (ref. **Fig. S15b)** and RCA catalysts exhibit relatively weak rate performance. Similarly, the specific capacities of the ZABs discharged at 5 mA cm^{-2} (see Fig. 4**c and Fig. S15c**) also follow the same sequence of Pt/C + RuO_2 (723 mAh/g) > RCA-30 (640 mAh g_{Zn}^{-1}) > RCA-15 (595 mAh g_{Zn}^{-1}) > SP-30 (591 mAh g_{Zn}^{-1}) > RCA (579 mAh g_{Zn}^{-1}).

Fig. 4**d** manifests that the ZAB with the RCA-30 catalyst exhibits a high peak power density of 92 mW cm^{-2} at 0.47 V, that is much larger than those with the SP-30 (59 mW cm^{-2}) and RCA (48 mW cm^{-2}) catalysts but is still weaker than the ZAB with the Pt/C + RuO_2 (115 mW cm^{-2}). **Fig. S15d** displays that the ZAB with the RCA-15 catalyst exhibits the highest peak power density of 66 mW cm^{-2} at 0.41 V. Fig. 4**e** illustrates the cyclic performance of the ZABs with the RCA-30, RCA, SP-30 and Pt/C + RuO_2 catalysts at a current density of 5 mA cm^{-2}. It is seen that the charge/discharge gap of the RCA-30 based ZAB (brown) is narrower than those with the RCA (green) and SP-30 (blue), where the insets highlight the stable charge/discharge cycles at the regions of 10-20 h and 60-70 h. As a result, the RCA-30 based ZAB exhibits a maximum cycle number of no less than 100 h, while the RCA and SP-30 based ZABs drop down to 95 h and 77 h, respectively, highlighting the effect of the activated recovered conductive agent on oxygen catalysis. In contrast, the Pt/C + RuO_2 based ZAB can also cycle for more than 100 h, and the charge/discharge gap remains narrower than the one with the RCA-30.

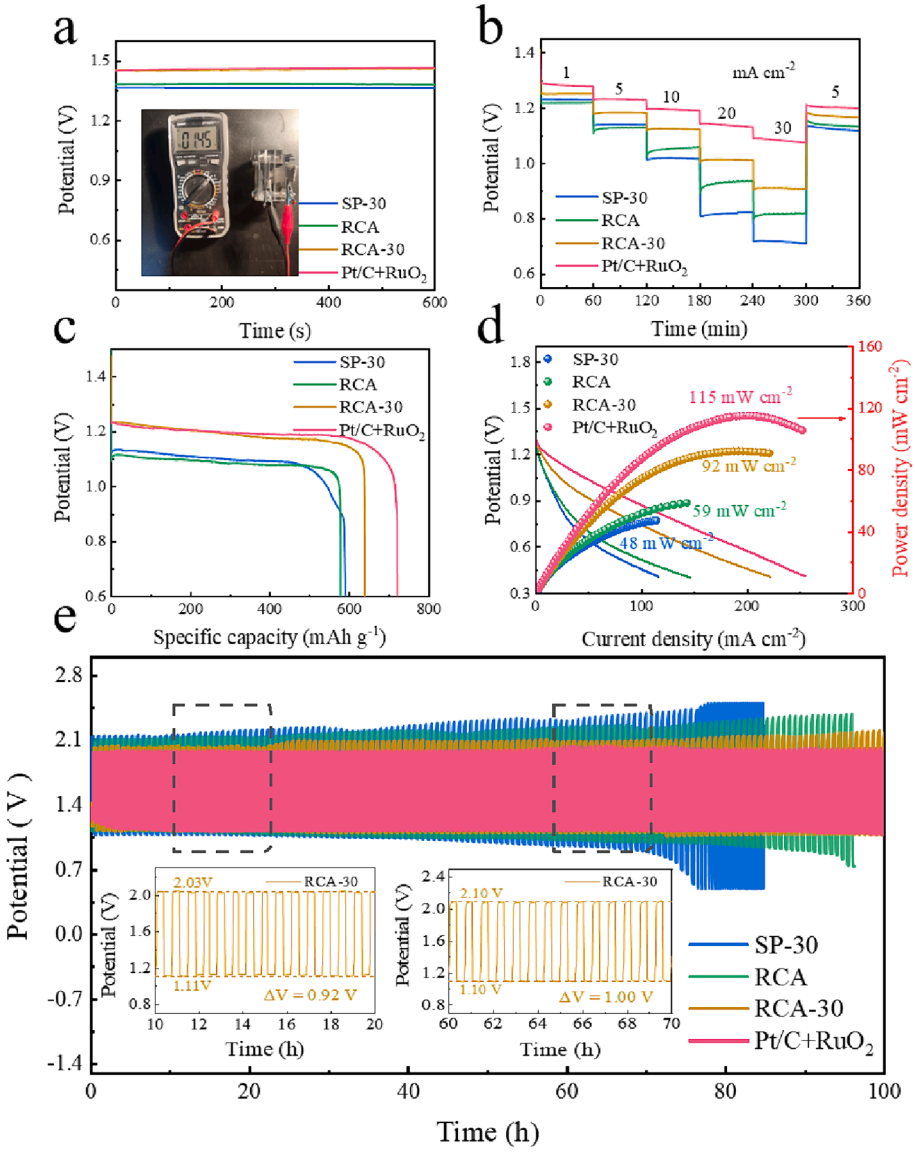

Fig. 4. Electrochemical performance of ZABs with the SP-30, RCA, RCA-30 and Pt/C + RuO_2 catalysts: (a) open circuit voltages (OCVs); (b) rate performance; (c) specific capacities at 5 mA cm^{-2}; (d) discharge polarization and power density curves; (e) discharge/charge curves at 5 mA cm^{-2} (40 min for each cycle), inset: cyclability with the RCA-30 catalyst from 10 h to 20 h and from 60 h to 70 h.

Table S5 shows that the ZAB with the RCA-30 catalyst is with comparable catalytic activity and stability to those with heteroatom doped carbon catalysts in previous reports but is still weaker than the noble metal Pt/C + RuO_2 catalyst. However, converting leaching waste to a high value-added bifunctional catalyst is of strong competitiveness in the aspects of material cost and resource sustainability, and cold plasma treatment allows for rapid batch processing of recovered conductive agents (RCAs) in spent LIBs.

4. Conclusion

We present a novel strategy for value-added utilisation of the leaching waste (recovered conductive agent, RCA) in chemical recovery of spent NCM-701515 LIBs. Nitrogen cold plasma bombardment at low pressure enables the nitrogen doping of carbon frameworks and activates the remained metal oxides (containing Ni and small amounts of Co, Mn elements) on the surface by decreasing their crystal size and exposing more active sites, rendering them efficient ORR/OER bifunctional electrocatalysts. When used in ZABs, the RCA-30 catalyst demonstrates a notable power density of 92 mW cm^{-2} and a cycle time of up to 100 h at a current density of 5 mA cm^{-2}, together with optimized rate performance and specific capacity. The catalytic performance of the RCA is prospective to be upgraded when Ni, Co and Mn can be co-doped with nitrogen into carbon frameworks in our future work. The nitrogen cold plasma treatment allows for rapid batch processing of RCAs to prepare low-cost bifunctional catalysts, which presents a compelling approach for repurposing spent LIBs materials in the applications of metal-air batteries, water splitting, fuel cells, and supercapacitors.

CRediT authorship contribution statement

Yifan Liu: Writing – original draft, Formal analysis, Data curation, Conceptualization. **Xiangqun Zhuge:** Supervision. **Tong Liu:** Visualization, Formal analysis, Data curation. **Zhihong Luo:** Supervision. **Kun Luo:** Writing – review & editing, Visualization, Resources, Formal analysis, Conceptualization. **Yibing Li:** Visualization, Supervision, Funding acquisition. **Yurong Ren:** Supervision. **Maryam Bayati:** Writing – review & editing, Supervision. **Xiaoteng Liu:** Writing – review & editing, Resources, Formal analysis, Conceptualization.

Declaration of competing interest

The authors declare that they have no known competing financial interests or personal relationships that could have appeared to influence the work reported in this paper.

Data availability

Data will be made available on request.

Acknowledgement

The authors gratefully acknowledge the financial support from the National Natural Science Foundation of China (No. 51874051 and 52111530139), Jiangsu Specially-Appointed Professor Fund by Jiangsu Education Department, Engineering and Physical Sciences Research Council (No. EP/S032886/1), and RSC research grant (R21-220003).

Appendix A. Supplementary data

Supplementary data to this article can be found online at https://doi.org/10.1016/j.jcis.2024.03.169.

References

[1] C.-H. Jung, H. Shim, D. Eum, S.-H. Hong, Challenges and recent progress in $LiNi_xCoyMn_{1-x-y}O_2$ (NCM) cathodes for lithium ion batteries, J. Korean Ceram. Soc. 58 (2021) 1–27.
[2] Y. Xia, J.M. Zheng, C.M. Wang, M. Gu, Designing principle for Ni-rich cathode materials with high energy density for practical applications, Nano Energy 49 (2018) 434–452.
[3] Y. Shi, M.H. Zhang, Y.S. Meng, Z. Chen, Ambient-pressure relithiation of degraded $Li_xNi_{0.5}Co_{0.2}Mn_{0.3}O_2$ ($0 < x < 1$) via eutectic solutions for direct regeneration of lithium-ion battery cathodes, Adv. Energy Mater. 9 (2019) 1900454.
[4] X.L. Zeng, J.H. Li, B.Y. Shen, Novel approach to recover cobalt and lithium from spent lithium-ion battery using oxalic acid, J. Hazard. Mater. 295 (2015) 112–118.
[5] M. Fan, X. Chang, Q.H. Meng, L.-J. Wan, Y.-G. Guo, Progress in the sustainable recycling of spent lithium-ion batteries, SusMat 1 (2021) 241.
[6] J.H. Fang, Z.P. Ding, Y. Ling, J.P. Li, X.Q. Zhuge, Z.H. Luo, Y.R. Ren, K. Luo, Green recycling and regeneration of $LiNi_{0.5}Co_{0.2}Mn_{0.3}O_2$ from spent Lithium-ion batteries assisted by sodium sulfate electrolysis, Chem. Eng. J. 440 (2022) 135880.
[7] W.-S. Chen, H.-J. Ho, Recovery of valuable metals from lithium-ion batteries NMC cathode waste materials by hydrometallurgical methods, Metals 8 (2018) 321.
[8] E. Fan, L. Li, Z.P. Wang, J. Lin, Y.X. Huang, Y. Yao, R.J. Chen, F. Wu, Sustainable recycling Technology for Li-ion Batteries and beyond: challenges and future prospects, Chem. Rev. 120 (2020) 7020–7063.
[9] G. Harper, R. Sommerville, E. Kendrick, L. Driscoll, P. Slater, R. Stolkin, A. Walton, P. Christensen, O. Heidrich, S. Lambert, A. Abbott, K. Ryder, L. Gaines, P. Anderson, Recycling lithium-ion batteries from electric vehicles, Nature 575 (2019) 75–86.
[10] X.H. Zheng, Z.W. Zhu, X. Lin, Y. Zhang, Y. He, H.B. Cao, Z. Sun, A mini-review on metal recycling from spent lithium ion batteries, Eng. 4 (2018) 361–370.
[11] H.-C. Li, Y.-J. Zhang, X. Hu, W.-J. Liu, J.-J. Chen, H.-Q. Yu, Metal-organic framework templated Pd@PdO–Co_3O_4 nanocubes as an efficient bifunctional oxygen electrocatalyst, Adv. Energy Mater. 8 (2018) 1702734.
[12] Y.J. Lee, S.H. Park, S.H. Kim, Y. Ko, K. Kang, Y.J. Lee, High-rate and high-areal-capacity air cathodes with enhanced cycle life based on RuO_2/MnO_2 bifunctional electrocatalysts supported on CNT for pragmatic Li−O_2 batteries, ACS Catal. 8 (2018) 2923–2934.
[13] H. Osgood, S.V. Devaguptapu, H. Xu, J. Cho, G. Wu, Transition metal (Fe, Co, Ni, and Mn) oxides for oxygen reduction and evolution bifunctional catalysts in alkaline media, Nano Today 11 (2016) 601–625.
[14] H.D. Xu, J. Yang, R.Y. Ge, J.J. Zhang, Y. Li, M.Y. Zhu, L.M. Dai, S. Li, W.X. Li, Carbon-based bifunctional electrocatalysts for oxygen reduction and oxygen evolution reactions: optimization strategies and mechanistic analysis, J. Energy Chem. 71 (2022) 234–265.
[15] Z.X. Zhang, P.L. Li, X. Zhang, C. Hu, Y.W. Li, B. Yu, N. Zeng, C. Lv, J.F. Song, M. C. Li, Recent advances in layered-double-hydroxides based Noble metal nanoparticles efficient electrocatalysts, Nanomaterials-Basel 11 (2021) 2624.
[16] K. Tang, C.Z. Yuan, Y. Xiong, H.B. Hu, M.Z. Wu, Inverse-opal-structured hybrids of N, S-codoped-carbon-confined Co_9S_8 nanoparticles as bifunctional oxygen electrocatalyst for on-chip all-solid-state rechargeable Zn-air batteries, Appl. Catal. B-Environ. 260 (2020) 118209.
[17] K. Luo, M. Zhou, T. Liu, X.Q. Zhuge, T.X.T. Liu, M. Bayati, Y.R. Ren, Z.H. Luo, A high-performance zinc-air battery cathode catalyst from recycling of spent lithium iron phosphate batteries, Small Struct. 4 (2023) 2300107.
[18] J.-S. Lee, S.T. Kim, R.G. Cao, N.-S. Choi, M.L. Liu, K.T. Lee, J. Cho, Metal-air batteries with high energy density: Li–Air versus Zn–Air, Adv. Energy Mater. 1 (2011) 34–50.
[19] F.-L. Meng, Z.-L. Wang, H.-X. Zhong, J. Wang, J.-M. Yan, X.-B. Zhang, Reactive multifunctional template-induced preparation of Fe-N-doped mesoporous carbon microspheres towards highly efficient electrocatalysts for oxygen reduction, Adv. Mater. 28 (2016) 7948–7955.
[20] K. Tang, H.B. Hu, Y. Xiong, L. Chen, J.Y. Zhang, C.Z. Yuan, M.Z. Wu, Hydrophobization engineering of the air-cathode catalyst for improved oxygen diffusion towards efficient zinc-air batteries, Angew. Chem. Int. Ed. 61 (2022) e202202671.
[21] M.L. Jiao, Q. Zhang, C.L. Ye, Z.B. Liu, X.W. Zhong, J.X. Wang, C. Li, L.X. Dai, G. M. Zhou, H.-M. Cheng, Recycling spent $LiNi_{1-x-y}Mn_xCo_yO_2$ cathodes to bifunctional NiMnCo catalysts for zinc-air batteries, Proc. Natl. Acad. Sci. 119 (2022).
[22] L.B. Di, J.S. Zhang, X.L. Zhang, H.Y. Wang, H. Li, Y.Q. Li, D.C. Bu, Cold plasma treatment of catalytic materials: a review, J. Phys. D. Appl. Phys. 54 (2021) 333001.
[23] L. Xu, Q.Q. Jiang, Z.H. Xiao, X.Y. Li, J. Huo, S.Y. Wang, L.M. Dai, Plasma-engraved Co_3O_4 nanosheets with oxygen vacancies and high surface area for the oxygen evolution reaction, Angew. Chem. Int. Ed. 55 (2016) 5277–5281.
[24] S.H. Park, J. Chae, M.-H. Cho, J.H. Kim, K.-H. Yoo, S.W. Cho, T.G. Kim, J.W. Kim, High concentration of nitrogen doped into graphene using N_2 plasma with an aluminum oxide buffer layer, J. Mater. Chem. C 2 (2014) 933–939.
[25] X. Lia, B.W. Zhang, X.M. Yan, Y. Zhang, X.Q. Deng, S. Zhang, Fe, N-doped graphene prepared by NH3 plasma with a high performance for oxygen reduction reaction, Catal. Today 337 (2019) 97–101.
[26] P. Rao, D.X. Wu, J.M. Luo, J. Li, P.L. Deng, Y.J. Shen, X.L. Tian, A plasma bombing strategy to synthesize high-loading single-atom catalysts for oxygen reduction reaction, Cell Rep. Phys. Sci. 3 (2022) 100880.
[27] X.T. Liu, K. Zhang, J.W. Lu, K. Luo, J.L. Gong, V.K. Puthiyapura, K. Scott, Determining the effect of plasma pre-treatment on antimony tin oxide to support Pt@Pd and the oxygen reduction reaction activity, ChemCatChem 7 (2015) 1543–1546.
[28] P.P. Su, H. Xiao, J. Zhao, Y. Yao, Z.G. Shao, C. Li, Q.H. Yang, Nitrogen-doped carbon nanotubes derived from Zn–Fe-ZIF nanospheres and their application as efficient oxygen reduction electrocatalysts with in situ generated iron species, Chem. Sci. 4 (2013) 2941–2946.
[29] L. Xu, G.Q. Zhang, J. Chen, Y.F. Zhou, G.E. Yuan, F.L. Yang, Spontaneous redox synthesis of Prussian blue/graphene nanocomposite as a non-precious metal catalyst for efficient four-electron oxygen reduction in acidic medium, J. Power Sources 240 (2013) 101–108.
[30] S.-M. Lee, S.-H. Lee, J.-S. Roh, Analysis of activation process of carbon black based on structural parameters obtained by XRD analysis, Crystals 11 (2021) 153.
[31] L. Li, Y.-J. Chen, H.-R. Xing, N. Li, J.-W. Xia, X.-Y. Qian, H. Xu, W.-Z. Li, F.-X. Yin, G.-Y. He, H.-Q. Chen, Single-atom Fe-N_5 catalyst for high-performance zinc-air batteries, Nano Res. 15 (2022) 8056–8064.
[32] P.Z. Chen, T.P. Zhou, L.L. Xing, K. Xu, Y. Tong, H. Xie, L.D. Zhang, W.S. Yan, W. S. Chu, C.Z. Wu, Y. Xie, Atomically dispersed iron-nitrogen species as electrocatalysts for bifunctional oxygen evolution and reduction reactions, Angew. Chem. Int. Ed. 56 (2017) 610–614.
[33] A. Ashok, A. Kumar, J. Ponraj, S.A. Mansour, F. Tarlochan, Highly active and stable bi-functional $NiCoO_2$ catalyst for oxygen reduction and oxygen evolution reactions in alkaline medium, Int. J. Hydrogen Energy 44 (2019) 16603–16614.
[34] P.T. Liu, J.Q. Ran, B.R. Xia, S.B. Xi, D.Q. Gao, J. Wang, Bifunctional oxygen electrocatalyst of mesoporous Ni/NiO nanosheets for flexible rechargeable Zn–Air batteries, Nano-Micro Lett. 12 (2020) 68.
[35] X. Zhang, R.R. Liu, Y.P. Zang, G.Q. Liu, G.Z. Wang, Y.X. Zhang, H.M. Zhang, H. J. Zhao, Co/CoO nanoparticles immobilized on Co–N–doped carbon as trifunctional electrocatalysts for oxygen reduction, oxygen evolution and hydrogen evolution reactions, Chem. Comm. 52 (2016) 5946–5949.
[36] C.Q. Shang, M.Y. Yang, Z.Y. Wang, M.C. Li, M. Liu, J. Zhu, Y.G. Zhu, L.J. Zhou, H. Cheng, Y.Y. Gu, Y.G. Tang, X.Z. Zhao, Z.G. Lu, Encapsulated MnO in N-doping carbon nanofibers as efficient ORR electrocatalysts, Sci. China Mater. 60 (2017) 937.